JOURNAL OF THERMOPHYSICS AND HEAT TRANSFER
Vol. 16, No. 4, October–December 2002

Buoyancy and Marangoni Effects in an Evaporating Drop

R. Savino,* D. Paterna,† and N. Favaloro‡
Università di Napoli "Federico II," 80125 Naples, Italy

Experiments and numerical simulations are carried out to study Marangoni and buoyancy effects in a hanging evaporating drop. The liquids investigated are n-octane, which exhibits Marangoni effect, and water, which does not exhibit thermal Marangoni effect. The disk sustaining the drop (diameter of a few millimeters) is held at a constant temperature. A temperature difference arises in the droplet as a consequence of the energy exchange with the ambient and of the evaporative cooling. In the presence of surface tension gradients (Marangoni effect), convective flows are established, and small surface temperature differences are measured at the drop-ambient interface. When the thermal Marangoni effect is absent (as in the water droplet), the surface temperature is stratified, and much larger surface temperature differences are established over the drop surface. The velocity field inside the droplet is evaluated by monitoring the motion of tracers within the drop, in the meridian plane, using a charge-coupled device (CCD) camera. The surface temperature distribution is detected by an infrared camera. The average evaporation rate is measured by computing the liquid volume change, which is done by analyzing the digitized CCD image of the interface shape. The experimental observations are compared with the simulations obtained by a numerical code, solving the axisymmetric steady Navier–Stokes equations taking into account the presence of Marangoni shear stresses and evaporation cooling at the liquid–air interface. A good agreement is found between experimental and numerical results.

Nomenclature

c	=	mass fraction
D	=	mass diffusivity, m^2/s
g_r	=	radial component of gravity acceleration, m^2/s
g_φ	=	azimuthal component of gravity acceleration, m^2/s
H_c	=	latent heat of vaporization, J/kg
h	=	distance of the bottom point of the drop surface from the disk, m
J_c	=	evaporation mass flux, kg/s
M	=	molecular weight, kg/kgmol
Ma	=	Marangoni number
p	=	pressure, Pa
p_v	=	vapor pressure, Pa
p_v^*	=	equilibrium saturation pressure, Pa
R	=	droplet radius, m
R_a, R_v	=	gas constants for air and vapor, respectively, J/kg/K
r	=	radial coordinate, m
T	=	temperature, °C
t	=	time, s
u	=	radial component of velocity, m/s
V	=	velocity magnitude, m/s
$\mathcal{V}$	=	droplet volume, m^3
v	=	tangential component of velocity, m/s
x	=	axial coordinate, m
α	=	thermal diffusivity, m^2/s
β_T	=	thermal expansion coefficient, 1/K
ε	=	liquid emissivity
λ	=	thermal conductivity, W/m/K
μ	=	viscosity, kg/m/s
ν	=	kinematic viscosity, m^2/s
ρ	=	density, kg/m^3
σ	=	surface tension, N/m
τ	=	nondimensional time
φ	=	azimuthal coordinate
χ	=	molar fraction

Subscripts

g	=	gas phase
i	=	initial ($t = 0$)
l	=	liquid phase
v	=	vapor
0	=	reference conditions
∞	=	ambient conditions

I. Introduction

DROPLET vaporization, as a result of the large number of practical applications, has been the subject of a large number of analytical, experimental, and computational investigations. In fact, the phenomena associated with the evaporation and combustion of a single droplet are fundamental to the processes taking place in furnaces, gas turbine combustors, and internal combustion engines. The literature[1–7] includes several investigations dealing with droplet evaporation and combustion phenomena. However, most of the previous works have generally neglected the thermocapillary (Marangoni) effects on droplets evaporation process. Lozinsky and Matalon[8] studied the Marangoni effect on the internal flow in a spinning droplet without considering its effect on drop evaporation. Haywood et al.[9] analyzed the Marangoni effect on droplet vaporization in conjunction with droplet deformation. Only recently, Niazmand et al.[10] and Shih and Megaridis[11] addressed Marangoni flows in evaporating droplets only from a computational point of view. On the other hand, Chao and Zhang[12] investigated experimentally the effects of evaporation and Marangoni flows on the spreading of liquid droplets on a solid surface.

The authors have investigated Marangoni effects in different problems (for instance, wetting and drops coalescence prevention, behavior of drops in liquid matrices[13–16]).

In this work an experimental and numerical study of evaporation in hanging droplets is carried out, aimed at studying the influence of buoyancy and Marangoni effects on the vaporization rates, on the surface temperature distributions, and on the convective velocities. In particular, water droplets (which do not exhibit Marangoni effect)

Received 18 December 2001; revision received 22 April 2002; accepted for publication 22 April 2002.

*Associate Professor of Fluid Dynamics, Department of Space Science and Engineering; rasavino@unina.it.
†Research Scientist, Department of Space Science and Engineering.
‡Aerospace Engineer, Department of Space Science and Engineering.

and hydrocarbon droplets (which exhibit relatively high surface tension gradients and Marangoni flows) are examined. The analytical investigation identifies the most relevant parameters of the process; the computational study of the thermofluid-dynamic field in the droplet and in the surrounding ambient well correlates the experimental results.

II. Laboratory Experiments

A scheme of the experimental apparatus is shown in Fig. 1. The system consists of a cylindrical support whose temperature T_s can be controlled by a Peltier element and a power generator driven by a computer. A hanging droplet is formed by a microliter syringe and suspended to the support. A lower support can be used to study sessile drops. The temperatures of the droplet T_d are measured by an infrared thermocamera (Flir SC3000) operating in the long wave band. The resolution of the thermocamera is 0.1 K, and its sensitivity is 20 mK at 30°C.

The thermocamera measures the radiant energy emitted by an object in the (infrared) window in which the sensor of the thermocamera is sensitive (around 9 μm). The thermocamera is calibrated so that an internal software allows one to detect the temperature distribution once the surface emissivity is known. (For the liquids under investigation, a very careful preliminary analysis has been carried out to measure the liquid emissivity in the temperature range under examination, and the value of the emissivity ε is reported in Table 1.) The thermocamera has a standard 20-deg lens, but two additional close-up lens can be mounted to enlarge the field of view: with the first close-up lens the field of view is 34 × 25 mm at a 10-cm distance to the object; with the additional microscope lens the field of view is 10 × 7.5 mm at a distance of 3 cm. A number of tests have shown that the liquids employed (octane, water) are not transparent at the thermocamera wavelength, and therefore the observed temperature is that of the surface with very little contribution of the liquid immediately beneath the surface. The size of the drop is also monitored by a charge-coupled device (CCD) camera (lateral view). Tracers motion inside the droplet can be detected with a laser sheet illumination.

Once the drop is formed, a vertical temperature gradient is established as a result of the evaporation (even if the disk temperature is equal to the ambient temperature); the disk temperature is higher than that of the lower part of the surface of the hanging drop, which cools as a result of the evaporation process and heat transfer with the ambient; a temperature gradient is therefore established along the drop surface. Because the surface tension at the liquid–air interface is a decreasing function of temperature, the particles along the liquid surface move toward the cold side, that is, toward the bottom, where the surface tension is higher. Because of continuity, in the central core of the drop, a vertical (fountain-like) upward flow takes place, which then returns to the bottom along the drop surface. Figure 2 shows the typical Marangoni flow pattern.

The liquids used for the experiments are n-octane and water. Table 1 shows the thermo-physical properties of these liquids at the temperature of 20°C and the corresponding properties of the vapor phases. Even though the temperature derivative of the surface tension of pure water is $\sigma_T = 10^{-4}$ N/m/K, Marangoni flows are not generally observed in water droplets because of the presence of impurities (surfactants), as discussed next; therefore, no surface tension gradients have been considered for all calculations that refer to water droplets.

Table 1 Properties at reference conditions (T_0 = 20°C)

Property	Octane liquid	Water	Octane vapor	Water vapor
ρ, kg/m^3	698.2	998.2	4.84	0.554
c_p, J/kg/K	2,420	4,182	2,467	2,014
λ, W/m/K	0.147	0.6	0.0178	0.0261
μ, kg/m/s	0.00054	0.001	6.75e−6	1.34e−5
D, m^2/s	——	——	6e−6	3e−5
H_c, J/kg	364,000	2,263,000	——	——
β_T, 1/K	0.0012	0.00025	——	——
σ_T, N/m/K	9.35e−5	10^{-4} (zero for all calculations)	——	——
ε	0.82	0.96	——	——
M, kg/kmole	114.2	18	114.2	18

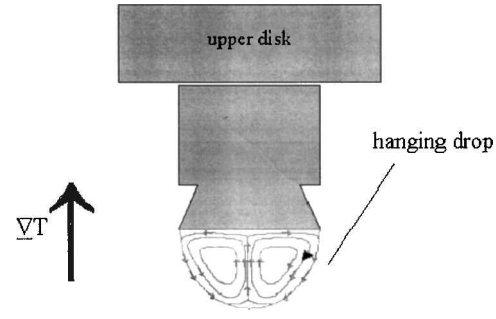

Fig. 2 Scheme of the hanging drop with Marangoni flows.

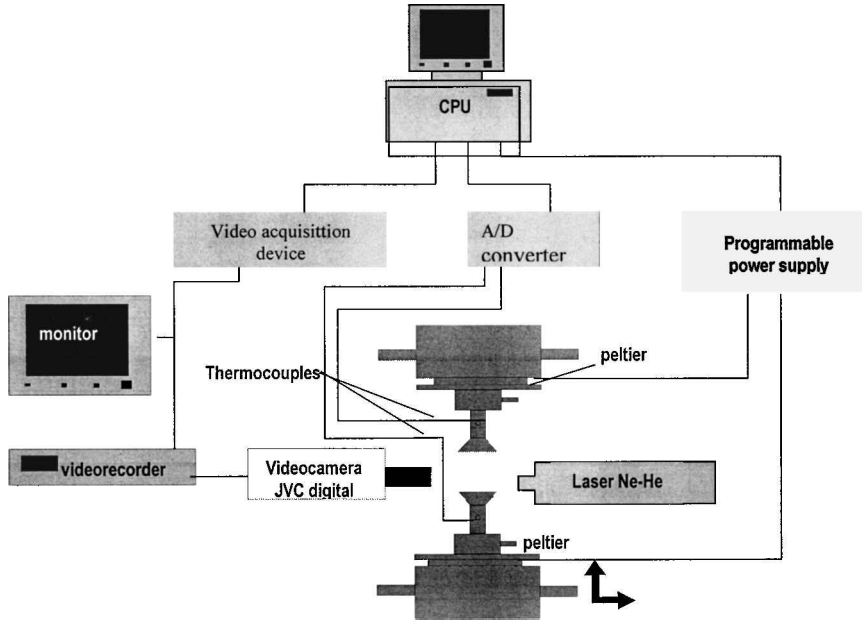

Fig. 1 Scheme of the experimental apparatus.

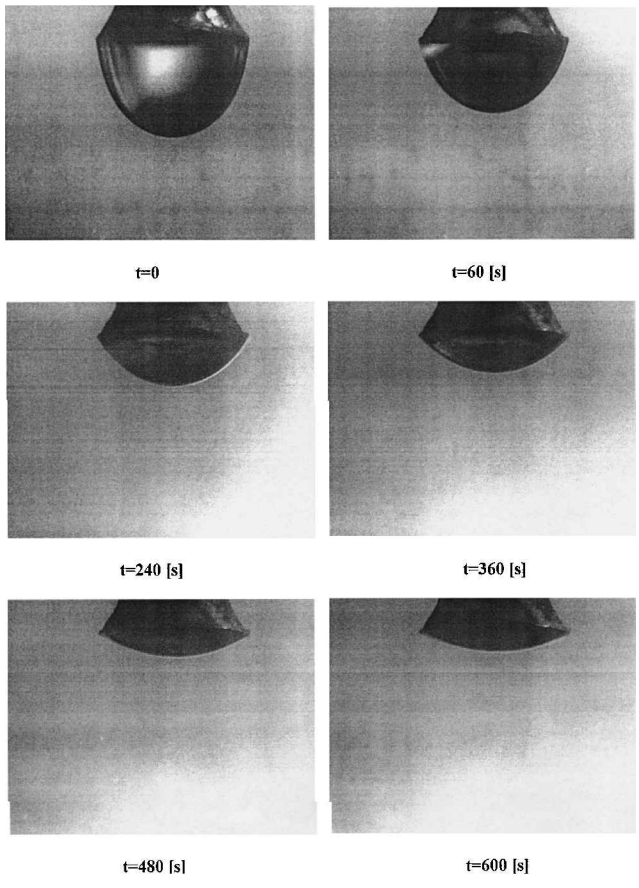

Fig. 3 Images of n-octane droplet during evaporation at $T_s = 22°$ C.

A number of experiments have been carried out at different temperatures of the disk ($R = 1.5$ mm) supporting the drop (initially at ambient temperature). During the experiments, the relative humidity in the surrounding air was measured and found to be approximately equal to 50%. Images of a n-octane hanging droplet during evaporation (lateral view) are shown in Fig. 3. The support is at ambient temperature ($T_s = 22°$C). The octane droplet evaporates in about 600 s. The pictures show how the droplet remains anchored to the disk edge; this is therefore the boundary condition imposed during the numerical computations. Tracers with diameter of about 20 μm have been used to observe the convective motion inside the drop, illuminating a meridian plane with a laser sheet (less than 1 mm thick). Figure 4 shows the tracers motions, at different times, during the evaporation process, for the same cases of Fig. 3. Each picture shows the streak lines displayed by the tracers in an exposure time of 0.02 s. The convective fields correspond to the flow pattern depicted in Fig. 2. The surface temperature distributions detected by the infrared thermocamera at two different temperatures of the copper disk ($T_s = 22°$C and 40°C) are shown in Fig. 5. The thermographs show that small temperature differences occur at the surface of a n-octane droplet. The maximum surface temperature difference is $\Delta T \cong 0.7$ K for $T_s = 22°$C (see Fig. 5a), corresponding to a Marangoni number $Ma = \sigma_T \Delta T \cdot R/(\mu \cdot \alpha) = 2090$, and $\Delta T \cong 4$ K, corresponding to $Ma = 11941$ for $T_s = 40°$C (see Fig. 5b).

For the water drop much lower rates of evaporation are observed at the same temperatures. For example, at $T_s = 22°$C the water droplet evaporates in about 3600 s. Furthermore, contrary to the octane drop, no motion is observed in the water droplet (the water–air interface does not exhibit Marangoni effect). As just mentioned, this behavior is explained by the properties of water that are affected by the presence of absorbed (or "surface active") impurities causing contamination of the water–air interface. In the present work no special care was taken to avoid contamination of the water drops because the objective of the research was to compare a drop (octane) exhibiting Marangoni effect with a drop (water) without Marangoni

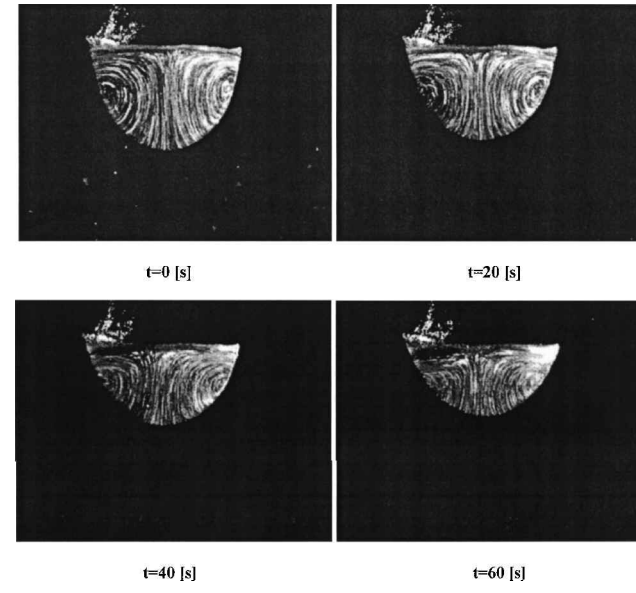

Fig. 4 Tracers trajectories in the octane droplet at $T_s = 22°$ C.

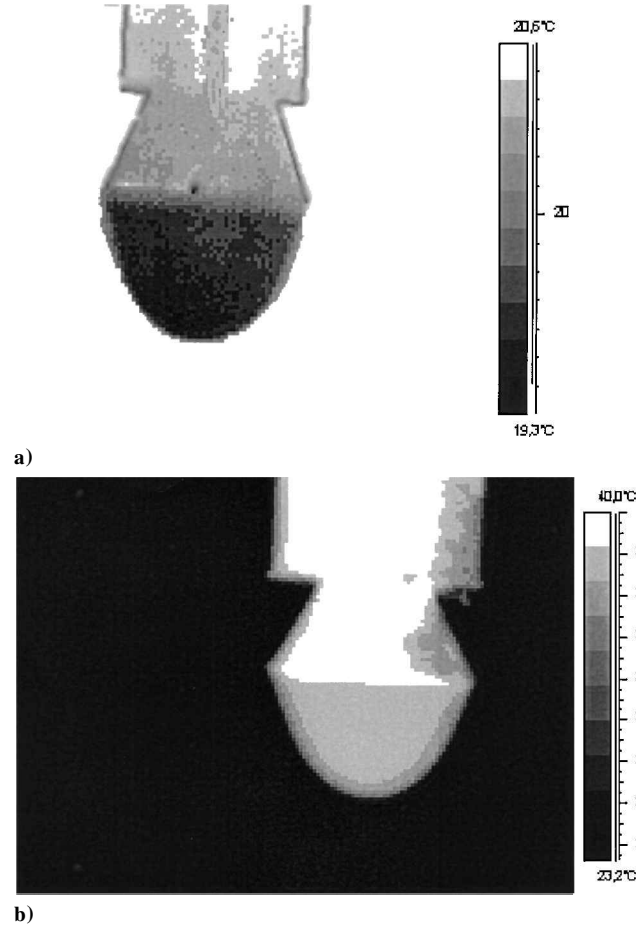

Fig. 5 Thermographic images of the octane droplet at a) $T_s = 22°$C and b) $T_s = 40°$C.

effect. Figure 6 shows the surface temperature of water droplets for $T_s = 22°$C and 40°C. The temperature is almost stratified, and the temperature differences are much higher than in the corresponding cases for octane ($\Delta T \cong 2.5$ K for $T_s = 22°$C, Fig. 6a; $\Delta T \cong 10$ K for $T_s = 40°$C, Fig. 6b). The problem investigated here is different from the typical works on drop evaporation and combustion,[17,18] where perfectly spherical drops in a hot environment are studied, because the spherical shape does not change during evaporation.

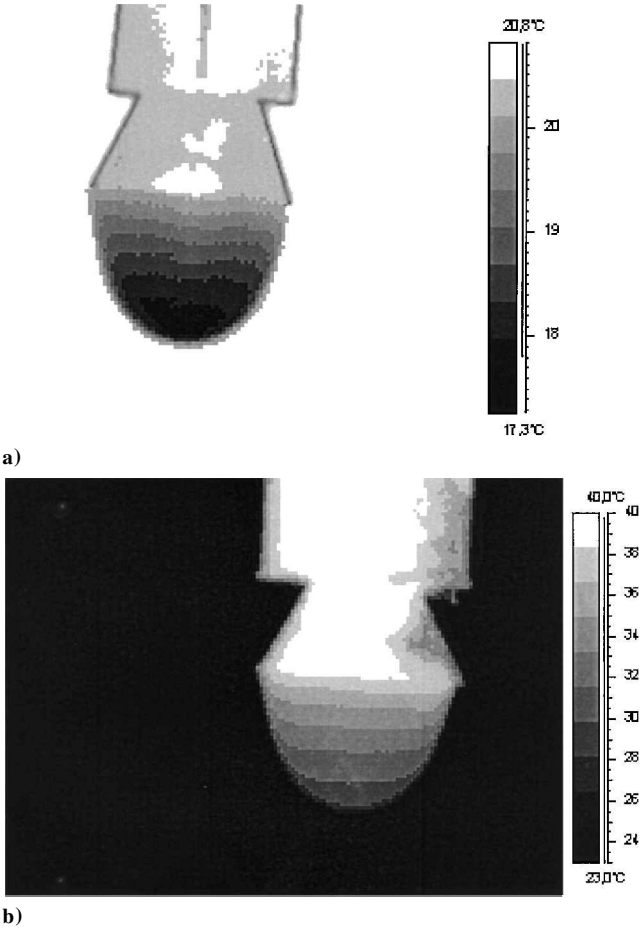

Fig. 6 Thermographic images of the water droplet at a) $T_s = 22°$ C and b) $T_s = 40°$ C.

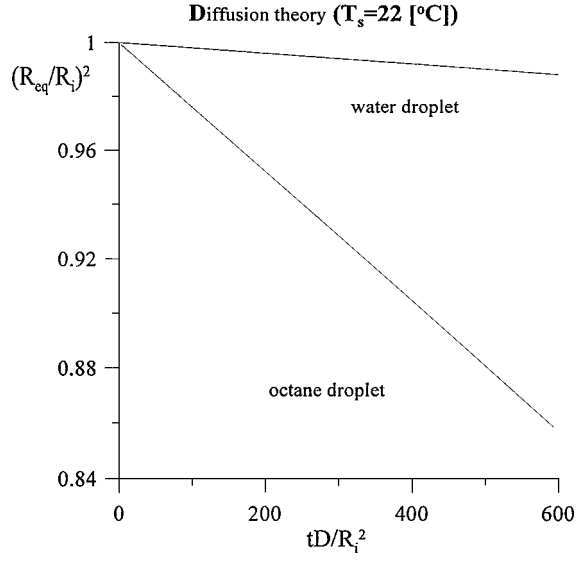

Fig. 7 Time profiles of quadratic regression rates for water droplet.

In our case, because the drop is attached to the disk it does not remain hemispherical during its evaporation (as is clearly shown in Fig. 3).

The height h and the volumes of the droplets at different times during the evaporation process have been measured with dedicated software, analyzing the computerized images of the drop shape detected with the CCD camera. Figures 7 and 8 show the drop volume (nondimensionalized with respect to the initial volume) vs the nondimensional time and the ratios h/R_i and R_{eq}/R_i, where R_i is

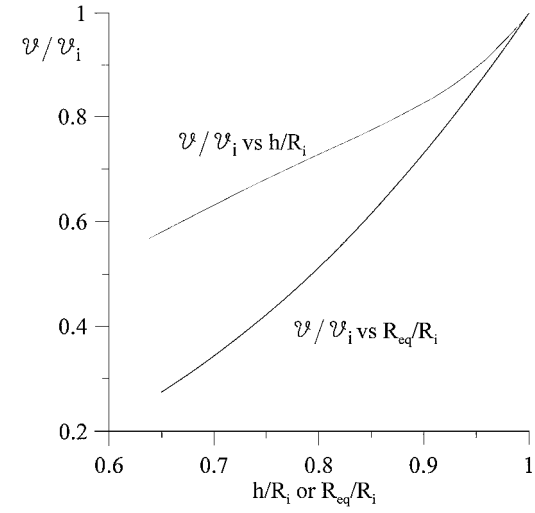

Fig. 8 Volume of the droplet as function of the droplet height and of the drop equivalent radius.

the radius of the hemispherical drop at the beginning of the evaporation process and R_{eq} is the radius of a hemispherical drop equivalent to the actual drop (that is, having the same volume of the droplet at the different times during evaporation):

$$R_{eq} = 3\sqrt{3\mathcal{V}/4\pi} \tag{1}$$

Figure 8 shows that the drop volume is proportional to the third power of R_{eq}, whereas, because of the nonspherical shape of the drop during the evaporation, the volume changes less rapidly with h. On the basis of the plot of Fig. 8, Figs. 9a and 9b show the ratio between the volume at time t and the initial volume at different temperatures of the disk for the droplets of octane and water, as functions of the nondimensional time τ (that is, the time divided by the characteristic diffusion time, $\tau = tD/R_i^2$, where D is the vapor diffusion coefficient in the surrounding air). The experimental values reported in this graph, as well as those shown in the subsequent figures, are plotted together with the uncertainty related to the accuracy and resolution of the visualization and acquisition system.

III. Diffusion Theory

The experimental results have been compared with the simplest analytical model, consisting in the purely diffusive evaporation of a spherical isothermal drop in an unbounded environment at constant vapor concentration. In this case the well-known quadratic law that gives the dependence of the evaporating drop radius vs time reads[19]

$$\frac{\mathrm{d}(R^2)}{\mathrm{d}t} = 2\frac{\rho_g}{\rho_l}\frac{D}{1-c_0}(c_\infty - c_0) \tag{2}$$

where c_0 and c_∞ are the vapor concentration at the drop interface and in the ambient, respectively.

Figure 7 shows the values of R^2 calculated by formula (2) for n-octane and water. The evaporation rate for a water droplet is smaller than that for octane, and this is in qualitative agreement with the experimental results, which show evaporation times for water (Fig. 9b) longer than those for octane (Fig. 9a). The different behavior between octane and water droplets, shown in Fig. 7, is related to the different thermo-physical properties of the investigated liquids (equilibrium saturation pressure, vapor diffusivity, density; see Table 1) and to the fact that the ambient is not dry but contains about 50% of relative humidity.

The equilibrium saturation pressures, in the investigated range of temperatures of water and n-octane, are shown in Fig. 10, where $p_v^*(T)$ is computed by the Clausius–Clapeyron law:

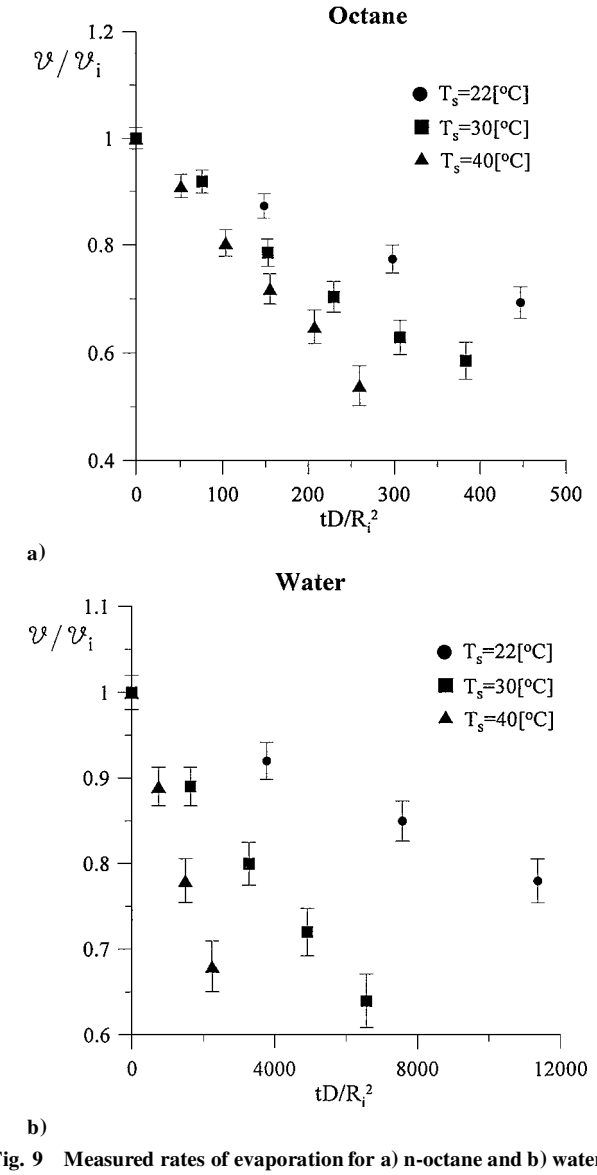

Fig. 9 Measured rates of evaporation for a) n-octane and b) water at different temperatures.

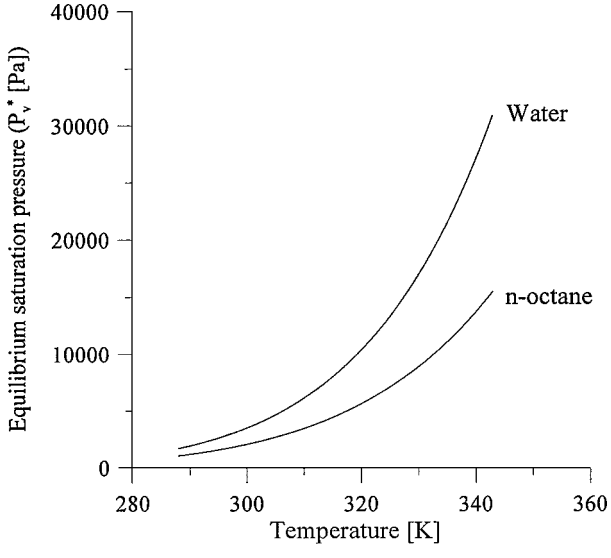

Fig. 10 Equilibrium saturation pressures for water and n-octane in the range 15–70° C.

$$p_v^*(T) = p_{v0}^* \exp\left[\frac{H_c}{R_g}\frac{(T - T_0)}{TT_0}\right] \tag{3}$$

Equation (3) shows that $p_v^*(T)$ increases with temperature with an exponential law. As shown in Fig. 10, the saturation pressure for water is higher than for n-octane in the investigated temperature range. However, the mass concentration at the drop–vapor interface c_0, which is directly related to the equilibrium saturation pressure,[7] is lower for water than for octane because of the higher molecular weight of octane (see Table 1). Even though the diffusive coefficient D for water is about five times the corresponding value for octane, the evaporation rate of octane is larger because the density ratio ρ_g/ρ_l is about $\frac{1}{6}$ of the corresponding value for octane (see Table 1) and because of a preexisting humidity in the ambient air. (For water at ambient temperature, $c_\infty/c_0 = 0.5$.)

The results of the diffusion theory are compared to the experimental results in Figs. 11 and 12. The diffusion theory strictly holds for a perfectly spherical drop, whereas, in this work, an anchored-drop geometrical configuration has been considered. In addition, for the octane droplet also convective effects are of great importance on the evaporation (see discussion in the Results paragraph), and the presence of the solid support (which represents an obstacle to the fluid motion) can change the results.

However, the experimental results exhibit the trend predicted by the diffusion theory (quadratic law), even if the results of the

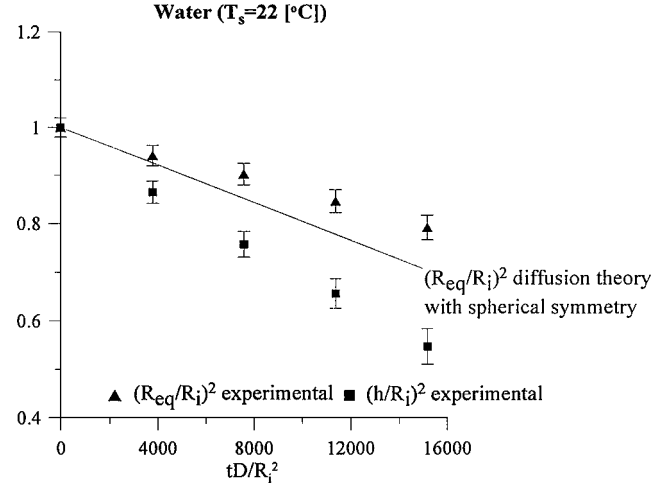

Fig. 11 Time profiles of regression rates for water droplet: ■, experimental $(h/R_i)^2$ and ▲, experimental $(R_{eq}/R_i)^2$.

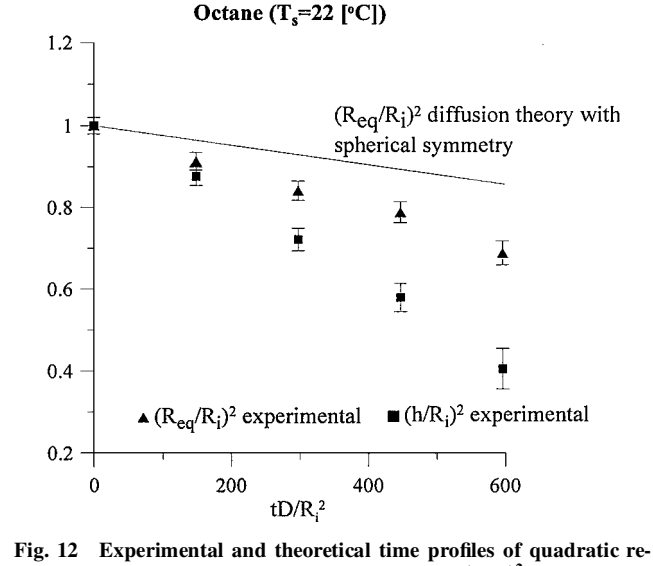

Fig. 12 Experimental and theoretical time profiles of quadratic regression rates for octane droplet: ■, experimental $(h/R_i)^2$ and ▲, experimental $(R_{eq}/R_i)^2$.

diffusion theory are not in quantitative agreement with the experimental results. In Fig. 11 the time profile of R^2 for the water droplet, as computed by Eq. (2), is compared with the measured values of the squared equivalent drop radius R_{eq}^2 for a water droplet at $T_s = 22°C$. In the same figure the time profile of h^2 is also shown (h being the distance, from the disk, of the bottom point of the droplet). Because the drop must remain anchored to the edge of the support, h decreases with time more rapidly than R_{eq}. Figure 11 also shows that the evaporation rate computed by Eq. (2) overestimates the effective evaporation rate $[d(R_{eq})/dt]$. This can be explained by the fact that R^2 is computed from Eq. (2) assuming the overall drop surface at the same temperature of the support, while the average drop temperature, and therefore the evaporation rate, decreases as a result of the evaporative cooling (see the thermographic images of Figs. 6). Figure 12 shows the same profiles as in Fig. 11 for the octane droplet. In this case, contrary to the preceding case, the rate of evaporation computed by Eq. (2) (at constant temperature) underestimates the effective evaporation rate.

This different behavior can be also explained by Marangoni and buoyancy convective effects prevailing in the octane droplet (as shown in Fig. 2). In fact, convective motions arise both in the droplet and in the surrounding ambient as a result of density and surface tension gradients. In this case the evaporation rate must be evaluated solving the full set of differential equations for the thermo-fluid-dynamic fields in the drop and in the surrounding ambient, as discussed in the following paragraph.

IV. Numerical Model

The model geometry and coordinate system is illustrated in Fig. 13. The effects of moving surface caused by the evaporation are supposed to be negligible (quasi-stationary evaporation), and therefore the liquid–air interface is considered fixed and undeformable. The assumption of a motionless droplet surface, which cannot describe the mass loss caused by the evaporation, is not a drawback because the authors are focusing on small intervals of time at the earlier stages of the evaporation process. Because all of the other dynamic processes in the droplet and the surrounding environment are found to be much faster than the evaporation process, this can be considered as a quasi-steady process, and the droplet deformation can be neglected with respect to the initial drop shape. The surface tension exhibits a linear dependence on the temperature:

$$\sigma = \sigma_0 - \sigma_T (T - T_0) \tag{4}$$

with

$$\sigma_T = -\frac{d\sigma}{dT} \tag{5}$$

For the density in the liquid phase, a linear dependence is also assumed with the temperature:

$$\rho_l = \rho_{10}[1 - \beta_{lT}(T - T_0)] \tag{6}$$

The ambient surrounding the droplet is modeled as a gas mixture of air and vapor with density ρ_g defined by the sum of the air and the vapor densities:

$$\rho_g = \rho_a + \rho_v \tag{7}$$

where

$$\rho_a = p_a/R_a T = \rho_g(1 - c) \tag{8}$$

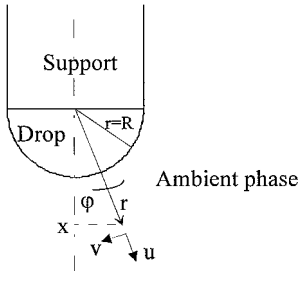

Fig. 13 Scheme of the model.

$$\rho_v = p_v/R_v T = \rho_g c \tag{9}$$

with p_a and p_v the partial pressures of air and vapor, respectively, and

$$p_a + p_v = p \tag{10}$$

The Boussinesq form of the mass, momentum, and energy conservation equations in polar coordinates read, in the liquid phase, as follows.

Continuity:

$$\frac{1}{r^2}\frac{\partial(r^2 u)}{\partial r} + \frac{1}{r\sin\varphi}\frac{\partial(v\sin\varphi)}{\partial\varphi} = 0 \tag{11}$$

Momentum along r:

$$u\frac{\partial(u)}{\partial r} + v\left(\frac{1}{r}\frac{\partial u}{\partial\varphi} - \frac{v}{r}\right) + \frac{1}{\rho_{10}}\frac{\partial p}{\partial r} = \nu_1\left[\nabla^2 u - 2\frac{u}{r^2} - \frac{2}{r^2\sin\varphi}\frac{\partial(v\sin\varphi)}{\partial\varphi}\right] + \frac{(\rho_1 - \rho_{10})}{\rho_{10}}g_r \tag{12}$$

Momentum along φ:

$$u\frac{\partial(v)}{\partial r} + v\left(\frac{1}{r}\frac{\partial v}{\partial\varphi} + \frac{u}{r}\right) + \frac{1}{\rho_{10}}\frac{\partial p}{\partial\varphi} = \nu_1\left(\nabla^2 u - 2\frac{v}{r^2\sin\varphi} + \frac{2}{r^2}\frac{\partial u}{\partial\varphi}\right) + \frac{(\rho_1 - \rho_{10})}{\rho_{10}}g_\varphi \tag{13}$$

Energy:

$$u\frac{\partial T}{\partial r} + \frac{v}{r}\left(\frac{\partial T}{\partial\varphi}\right) = \alpha_1\left[\frac{1}{r^2}\frac{\partial}{\partial r}\left(r^2\frac{\partial T}{\partial r}\right) + \frac{1}{r^2\sin\varphi}\frac{\partial}{\partial\varphi}\left(\sin\varphi\frac{\partial T}{\partial\varphi}\right)\right] \tag{14}$$

For the liquid phase, p is the difference between the actual and the hydrostatic pressure ($\rho_{10} g x$), and

$$\nabla^2 = \frac{1}{r^2}\frac{\partial}{\partial r}\left(r^2\frac{\partial}{\partial r}\right) + \frac{1}{r^2\sin\varphi}\frac{\partial}{\partial\varphi}\left(\sin\varphi\frac{\partial}{\partial\varphi}\right) \tag{15}$$

The liquid properties ρ_{10}, ν_1, α_1 can be obtained from Table 1.

For the gas phase the balance equations can be written as follows.

Continuity:

$$\frac{1}{r^2}\frac{\partial(r^2 u)}{\partial r} + \frac{1}{r\sin\varphi}\frac{\partial(v\sin\varphi)}{\partial\varphi} = 0 \tag{16}$$

Momentum along r:

$$u\frac{\partial(u)}{\partial r} + v\left(\frac{1}{r}\frac{\partial u}{\partial\varphi} - \frac{v}{r}\right) + \frac{1}{\rho_g}\frac{\partial p}{\partial r} = \nu_g\left[\nabla^2 u - 2\frac{u}{r^2} - \frac{2}{r^2\sin\varphi}\frac{\partial(v\sin\varphi)}{\partial\varphi}\right] + g_r \tag{17}$$

Momentum along φ:

$$u\frac{\partial(v)}{\partial r} + v\left(\frac{1}{r}\frac{\partial v}{\partial\varphi} + \frac{u}{r}\right) + \frac{1}{\rho_g}\frac{\partial p}{\partial\varphi} = \nu_g\left(\nabla^2 u - 2\frac{v}{r^2\sin\varphi} + \frac{2}{r^2}\frac{\partial u}{\partial\varphi}\right) + g_\varphi \tag{18}$$

Energy:

$$u\frac{\partial T}{\partial r}+\frac{v}{r}\left(\frac{\partial T}{\partial \varphi}\right)=\alpha_g\left[\frac{1}{r^2}\frac{\partial}{\partial r}\left(r^2\frac{\partial T}{\partial r}\right)+\frac{1}{r^2\sin\varphi}\frac{\partial}{\partial \varphi}\left(\sin\varphi\frac{\partial T}{\partial \varphi}\right)\right] \quad (19)$$

Species:

$$u\frac{\partial c}{\partial r}+\frac{v}{r}\left(\frac{\partial c}{\partial \varphi}\right)=D\left[\frac{1}{r^2}\frac{\partial}{\partial r}\left(r^2\frac{\partial c}{\partial r}\right)+\frac{1}{r^2\sin\varphi}\frac{\partial}{\partial \varphi}\left(\sin\varphi\frac{\partial c}{\partial \varphi}\right)\right] \quad (20)$$

The coupling between the flowfields in the liquid and gas phase is provided by the boundary conditions at the liquid-gas interface ($r=R, 0<\varphi<\pi/2$):

$$u=0 \quad (21)$$

$$\mu_1\left[\left(\frac{\partial v}{\partial r}\right)_{r=R}-\frac{v}{R}\right]_l-\mu_g\left[\left(\frac{\partial v}{\partial r}\right)_{r=R}-\frac{v}{R}\right]_g=\frac{1}{R}\frac{\partial \sigma}{\partial \varphi} \quad (22)$$

$$-\lambda_1\left(\frac{\partial T}{\partial r}\right)_{l(r=R)}=-\lambda_g\left(\frac{\partial T}{\partial r}\right)_{g(r=R)}+J_cH_c \quad (23)$$

$$c=c_0 \quad (24)$$

The condition (24) arises from the "phase equilibrium assumption," based on the fact that the evaporation is a very fast process compared with diffusion and convection in the ambient phase. The gas properties ν_g, α_g are computed as mass-weighted averages of the properties of air and vapor and are supposed to be constant with temperature.

The temperature of the support is uniform ($T=T_s$), and the diffusive flux of the vapor in the gas phase is zero. Symmetry conditions are applied on the axis.

Equations (11–14) and (16–20) have been solved with the conditions (21–24) using a finite volume method. The SIMPLE (semi-implicit method for pressure-linkedequations) family of algorithms

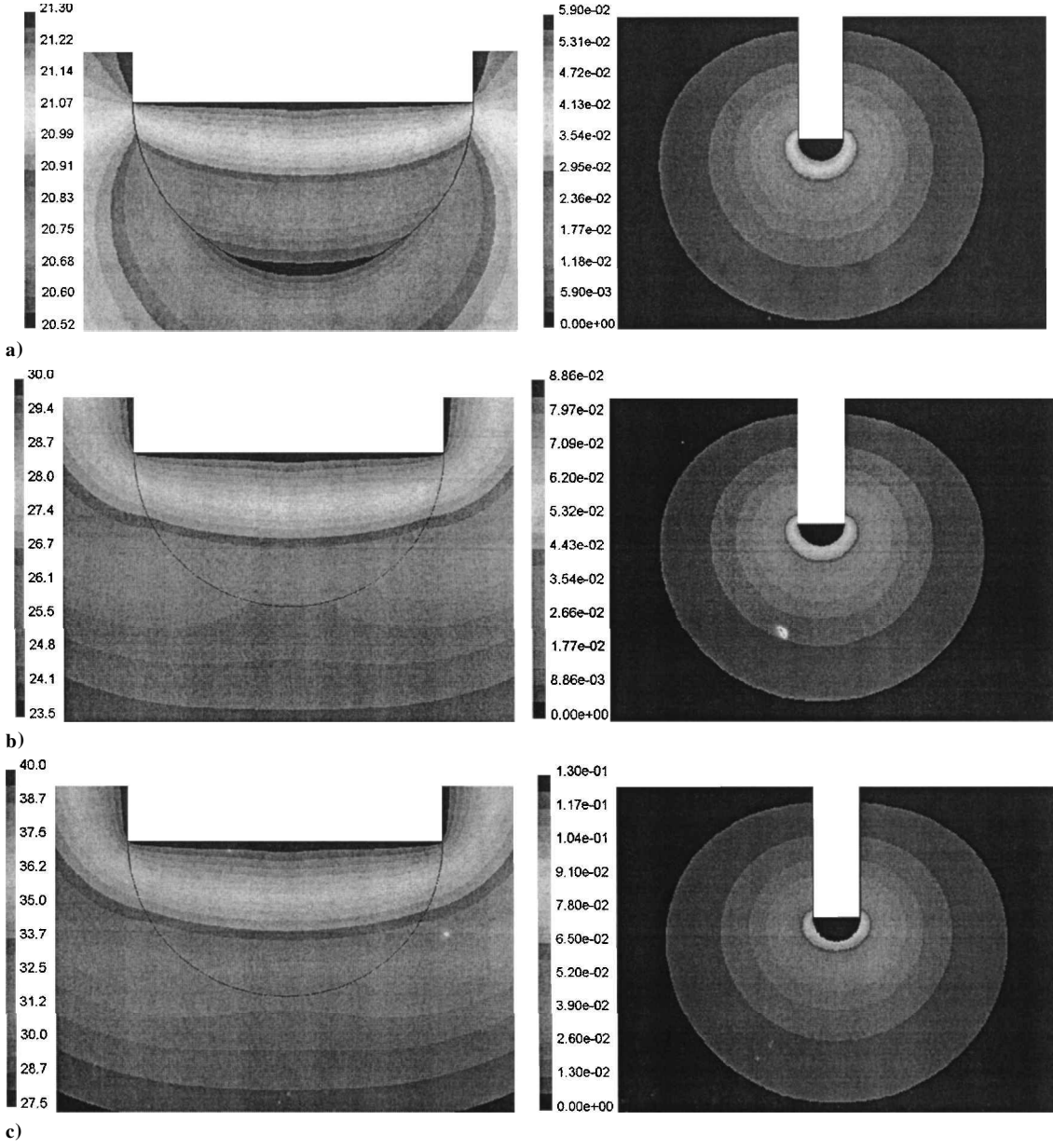

Fig. 14 Temperature (left) and species (right) distributions for the octane drop in purely diffusive conditions (no buoyancy, no Marangoni) at a) $T_s=22°C$, b) $T_s=30°C$, and c) $T_s=40°C$.

(Patankar[20] is used for introducing pressure into the continuity equation. Second-order upwind is used to discretize the momentum, energy, and species convective fluxes. Central schemes are used for diffusive fluxes. Typically, the number of quadrilateral cells used for the domain discretization is of the order of 15,000.

V. Influence of Convection on Drop Evaporation and Numerical-Experimental Correlation

To study the influence of convective motions on drop evaporation, different numerical simulations have been performed at the following conditions: 1) purely diffusive regime (no convection is present, that is, under zero gravity and absence of Marangoni stresses); 2) only Marangoni convection (for the octane droplet); 3) only buoyancy convection (for the water droplet); 4) Marangoni and buoyancy convection (for the octane droplet). All of the numerical simulations have been carried out assuming a hemispherical hanging drop anchored to a cylindrical disk of radius of 1.5 mm; therefore, all of the computations refer to early stages of the evaporation process, that is, when the droplet radius has not changed significantly with respect to its initial value. The corresponding experimental results, for comparison, refer to the times during the evaporation process when the hanging droplet is almost semispherical, with radius equal to the disk radius.

Figure 14 shows the temperature distribution in the octane droplet and in the surrounding air (left-hand side) and the distribution of the concentration of octane vapor around the drop (right-hand side), at different support temperatures ($T_s = 22°C$, 30°C, and 40°C) and in purely diffusive conditions. The temperature distribution inside the droplet is stratified, and the maximum temperature differences range from 1 K ($Ma = 2985$), for $T_s = 22°C$, to about 10 K ($Ma = 29{,}850$), for $T_s = 40°C$. This is clearly in disagreement with the temperature distribution detected by the thermographic images shown in Fig. 5 because the temperature field in the droplet is strongly influenced by buoyancy and Marangoni effects, as discussed next. The species mass fraction on the drop surface increases with temperature, and major differences are established along the surface at higher temperatures. In addition, the species distribution in the gas phase is almost sphero-symmetrical.

The numerical results for the water droplet (Fig. 15) exhibit similar behavior. In this case all calculations have been carried out assuming for ambient humidity the measured value of 50%. The

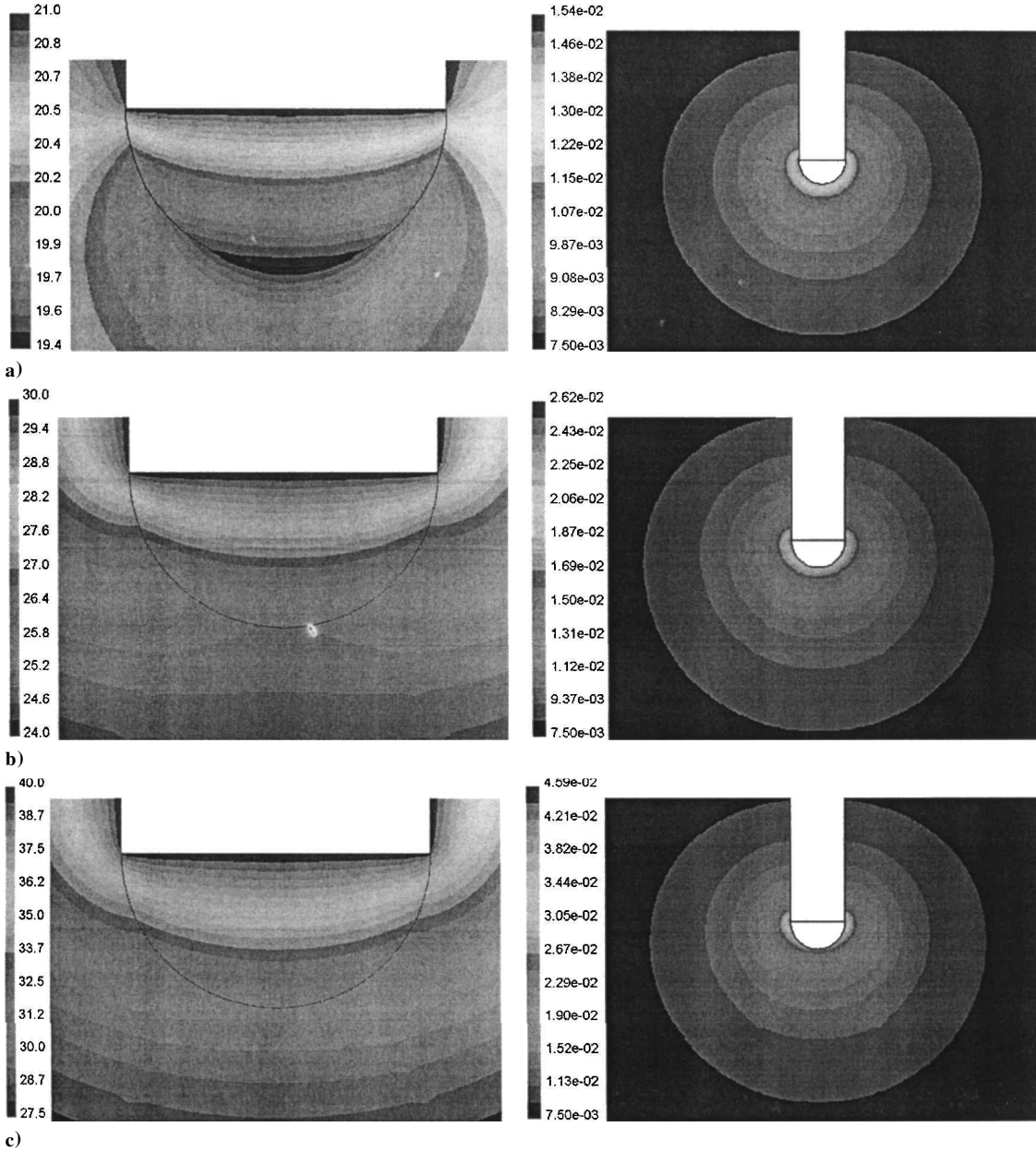

Fig. 15 Temperature (left) and species (right) distributions for the water drop in purely diffusive conditions (no buoyancy) at a) $T_s = 22°C$, b) $T_s = 30°C$, and c) $T_s = 40°C$.

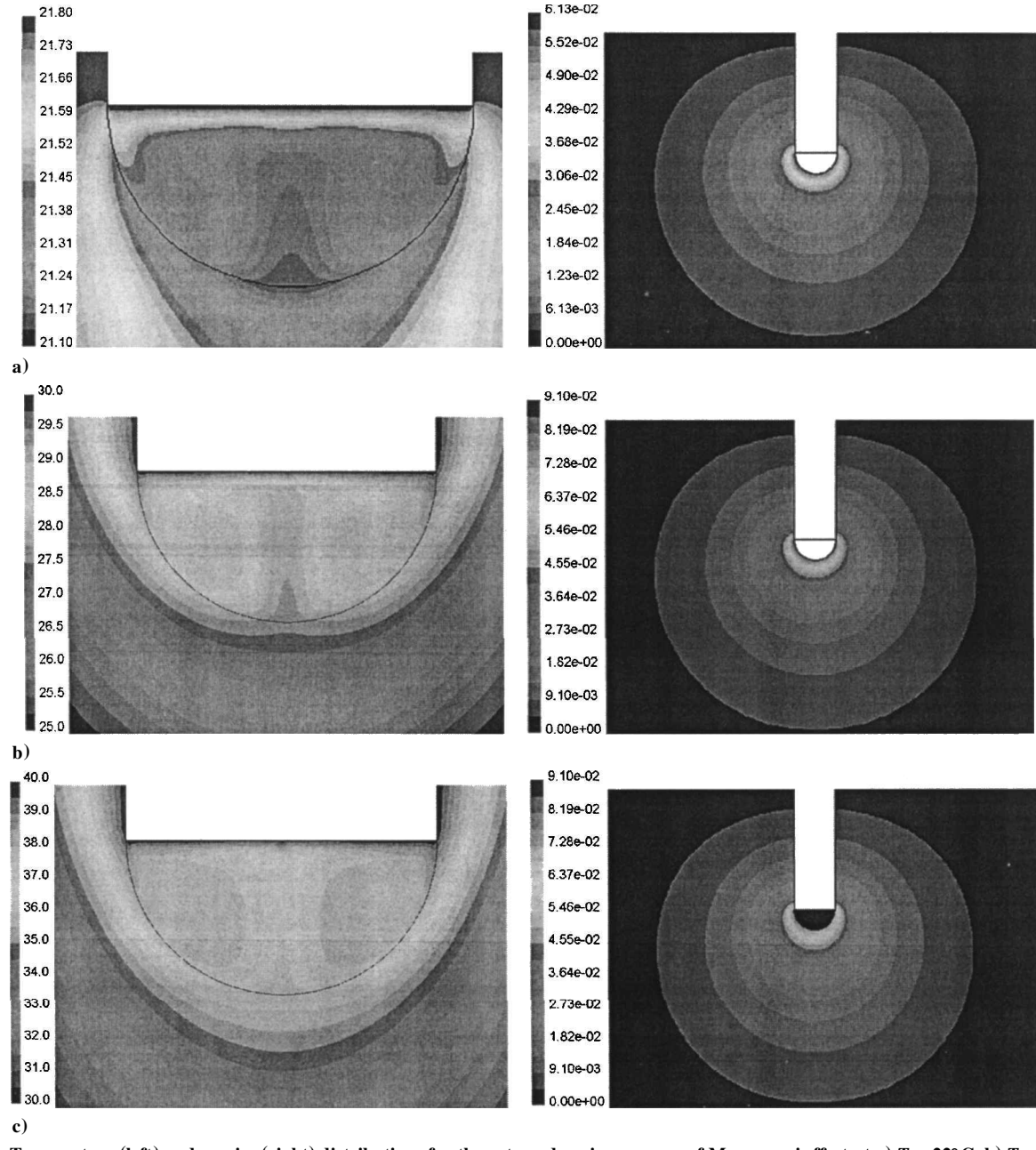

Fig. 16 Temperature (left) and species (right) distributions for the octane drop in presence of Marangoni effect at a) $T_s = 22°$ C, b) $T_s = 30°$ C, and c) $T_s = 40°$ C.

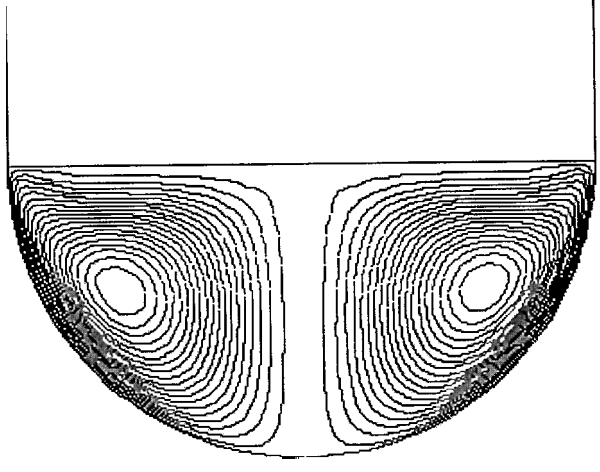

Fig. 17a Streamlines for the octane drop in the presence of Marangoni effect ($T_s = 40°$ C); max = 3.27×10^{-6} kg/s, min = 0, $\Delta = 3.3 \times 10^{-7}$ kg/s.

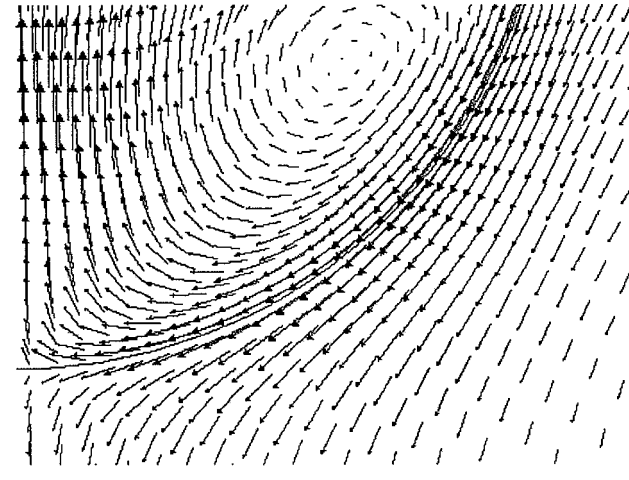

Fig. 17b Velocity vectors for the octane drop in presence of Marangoni effect ($T_s = 40°$ C); max = 2.88×10^{-2} m/s.

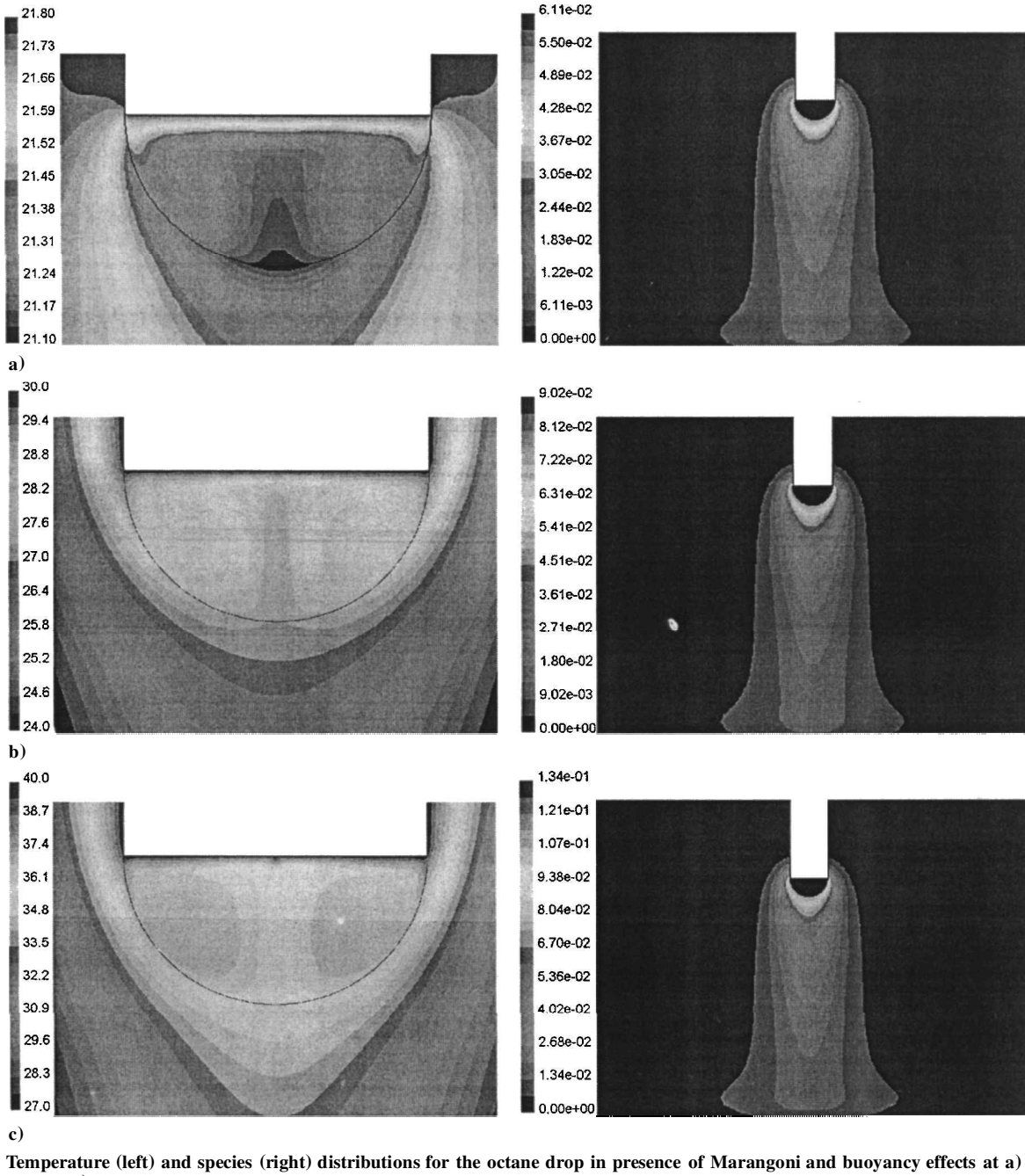

Fig. 18 Temperature (left) and species (right) distributions for the octane drop in presence of Marangoni and buoyancy effects at a) $T_s = 22°C$, b) $T_s = 30°C$, and c) $T_s = 40°C$.

temperature distribution is in sufficient agreement with the experimental measurements performed by the thermocamera (Fig. 6).

Figure 16 shows the computed temperature and species concentrations distributions for the octane droplet, when Marangoni effect is taken into account. As discussed before, in agreement with the experimental findings, the temperature difference along the drop surface, caused by the evaporative cooling, induces a surface motion (Marangoni flow) directed toward the lower surface temperature, which in turn drags fluid in the droplet and in the surrounding air. The temperature distribution is no longer stratified, but it is distorted by the axisymmetric thoroidal vortex induced by the surface flow (Fig. 17). In addition, the convective field causes a more uniform temperature, resulting in a smaller temperature difference with respect to the purely diffusive case. The temperature distributions on the drop surface appear now comparable with the experimental results (Fig. 5). Contrary to the isotherms in the droplet, the isoconcentration lines in the vapor phase are nearly unaffected by the flow induced by the surface motion.

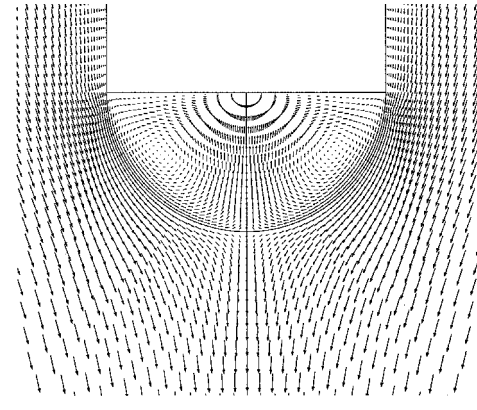

Fig. 19 Velocity vectors in the octane droplet and in the gas mixture as a result of Marangoni and buoyancy effects ($T_s = 40°C$). V_{max} = 0.09 m/s.

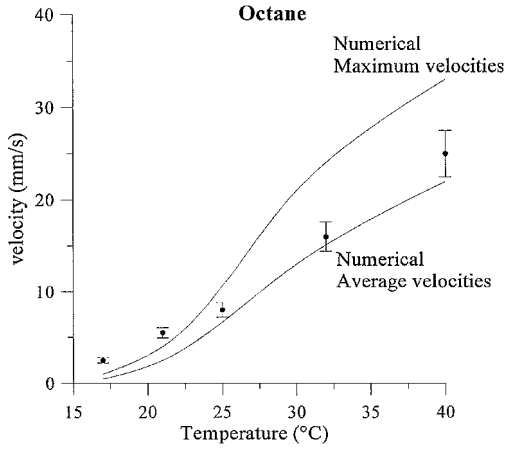

Fig. 20 Computed maximum and average velocities (along the symmetry axis) for the octane droplet and comparison with experimental data.

When buoyancy effects are also included, no noticeable differences appear in the drop, while the iso-concentrations in the surrounding ambient are highly distorted (compare Figs. 14 and 18). The buoyancy effects are of thermal and solutal nature. Apart from the case at ambient temperature, where the temperature differences in the gas phase are negligible, thermal and solutal buoyancy effects are counteracting. The hotter fluid near the liquid–gas interface tends to be directed upward, but, at the same time, the mixture is enriched with octane vapor, which is heavier than air and tends to be convected downward. The latter effect prevails, and a concentration plume is created below the drop on the symmetry axis. Velocities of the order of 10 cm/s are generated in the gas phase (Fig. 19).

Figure 20 shows the computed and measured velocities at different values of the support temperature. The maximum velocities computed along the symmetry axis of the drop are compared to the velocities measured, along the symmetry axis, by the tracers streaks, taking into account the CCD camera exposure time ($\frac{1}{50}$ s). Because the measured velocities are average values of the velocity in the exposure time, the average velocities along the symmetry axis have been also computed and reported for comparison in Fig. 20.

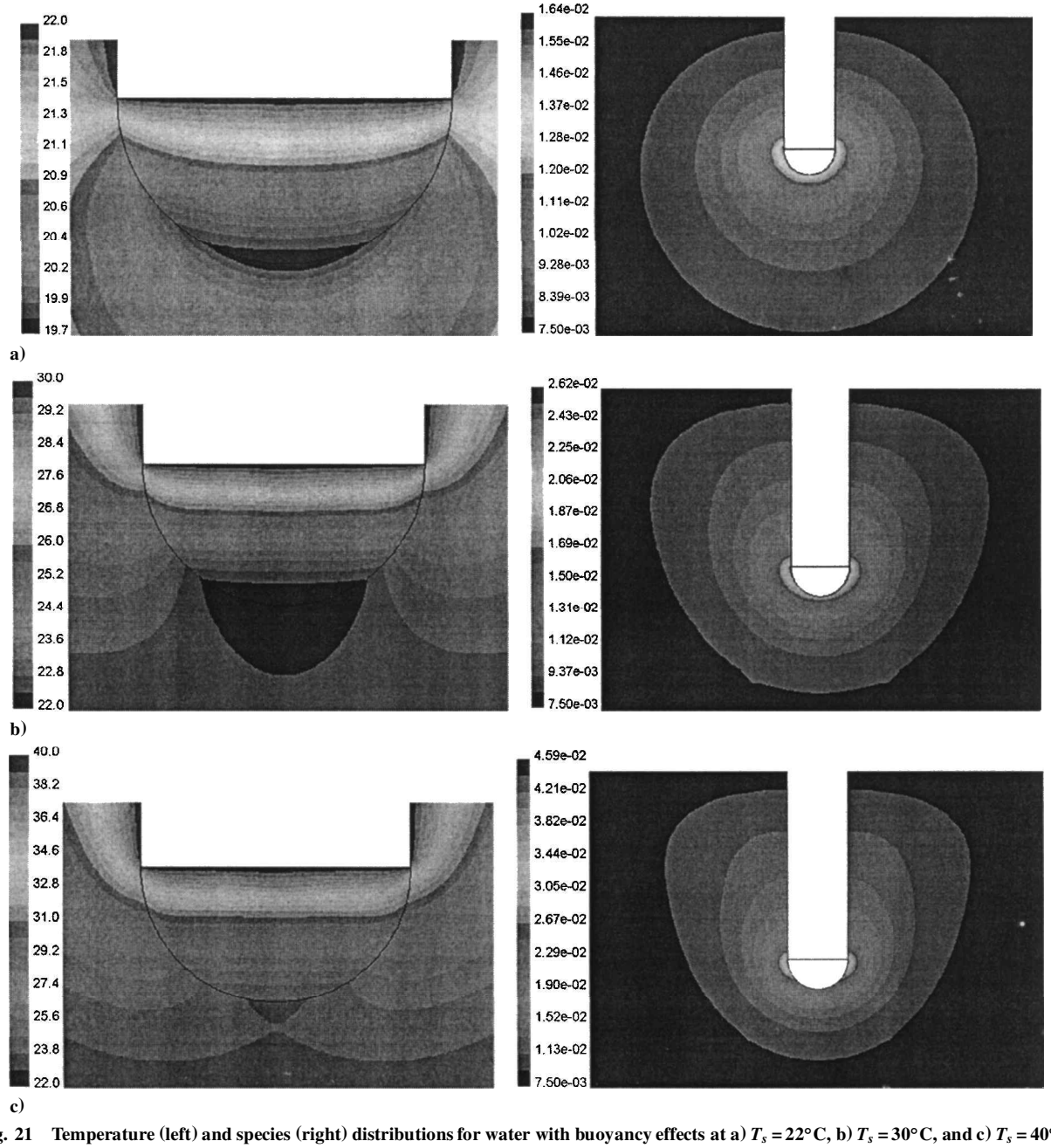

Fig. 21 Temperature (left) and species (right) distributions for water with buoyancy effects at a) $T_s = 22°C$, b) $T_s = 30°C$, and c) $T_s = 40°C$.

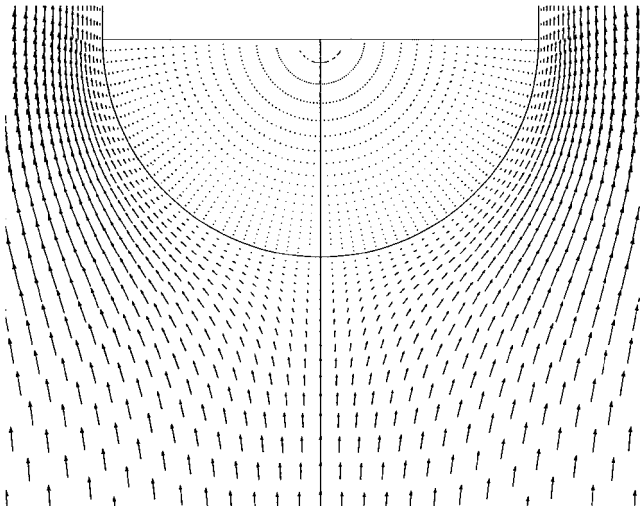

Fig. 22 Velocity vectors (m/s) in the ambient for the water droplet as a result of buoyancy effects ($T_s = 40°C$). $V_{max} = 1.65 \times 10^{-2}$ m/s.

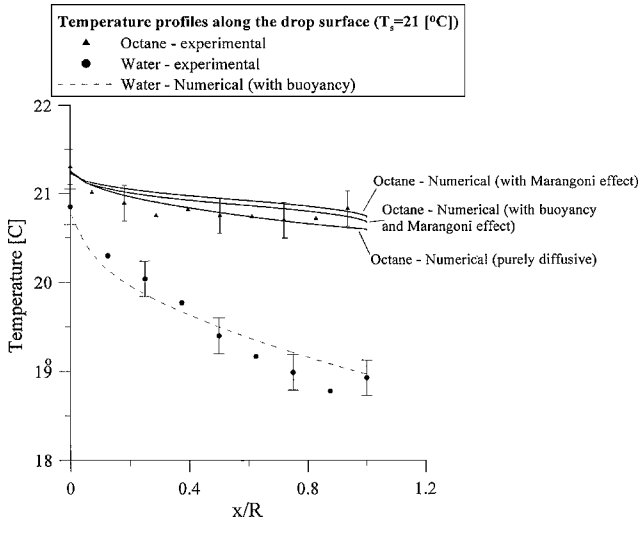

Fig. 23 Drop surface temperatures for n-octane and water droplets ($T_s = 21°C$).

For the water droplet, as already mentioned, Marangoni effects are negligible, and only buoyancy can play a role. Figure 21 shows the temperature and species concentrations for the water droplet when buoyancy effects are considered. In this case the gas mixture near the drop surface is lighter than air because 1) molecular weight of water vapor is lower than that of air (see Table 1) and 2) the temperature is higher (at least for support temperatures higher than the ambient temperature). Therefore the thermal and solutal buoyancy effects are concurrent and drive the fluid upward. At ambient temperature, because of the small density differences, the effect of buoyancy is negligible, while, increasing the support temperature, the flowfield appears much more distorted. The iso-concentration lines have an almost sphero-symmetrical distribution at ambient temperature, whereas at higher temperatures they show a plume-like feature near the bottom of the drop as a result of the motion in the ambient phase (Fig. 22).

The plot in Fig. 23 shows the temperature profiles along the drop surface for the octane and water drops at ambient temperature (at the early stages of the evaporation process). The contributions of Marangoni and buoyancy effects for the octane droplet are reported. Figure 23 shows that the temperature along the octane drop surface is almost uniform (maximum differences of the order of 0.6–0.7°C, $Ma \cong 2090$), whereas larger temperature differences are present along the water drop surface. This is mainly related to the different latent heat of vaporization between water and n-octane.

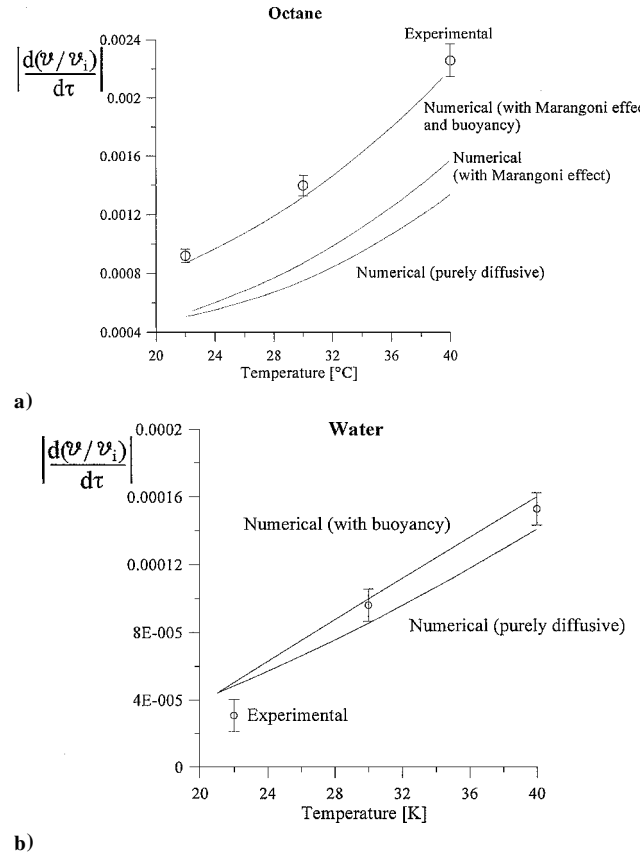

Fig. 24 Absolute value of the nondimensional evaporation rate vs temperature for a) octane and b) water droplets.

(The latent heat of vaporization of water is about seven times the one of octane; see Table 1.) Figure 23 also shows that, at ambient temperature, Marangoni and buoyancy effects on surface temperature distribution of octane droplet are not relevant.

However, Marangoni and buoyancy flows around the octane droplet highly affect the vaporization rates. In Figs. 24a and 24b the computed nondimensional rates of evaporation are compared with the experimental data. For the octane droplet the purely diffusive results do not correlate with the experimental data. Marangoni flows increase the evaporation rates by dragging the octane vapor away from the droplet and therefore increasing the species gradient on the drop surface, but their effect is not sufficient to explain the measured values. Better correlation with the experimental results is obtained including also buoyancy effects (inside the hanging drop and in the ambient atmosphere).

On the other hand, for the water droplet buoyancy effects are important at temperatures higher than the ambient temperature, whereas the purely diffusive results are sufficient to obtain a fair agreement with the experimental results at ambient temperature (Fig. 24b). In this case discrepancies from the diffusive theory are because, as already explained in Sec. III, the drop temperature is not uniform, but decreases along the drop surface.

VI. Conclusions

Experimental and numerical results on evaporating hanging drops of n-octane and water show that buoyancy and Marangoni convection affect the drop evaporation. The vaporization rates, the convective velocities, and the surface temperature distributions have been determined experimentally and correlated numerically. The main conclusions are summarized as follows:

1) The evaporation rates, for the water droplets, are smaller than those for octane droplets, even though the vapor pressure of water is higher than that of octane; this agrees with the numerical model when accounting for the different thermophysical properties of the two liquids and the ambient conditions.

2) The diffusion theory, based on the assumptions of isothermal and spherical drops, is not in agreement with the experimental results. Only numerical simulations of the thermo-fluid-dynamic field in the drop and in the surrounding ambient are able to correlate the experimental data. The numerical results are in agreement with the experimental ones only if the buoyancy and Marangoni effects are taken into account. For water droplets, which do not exhibit Marangoni effects, the influence of buoyancy is not so important as for octane drops.

3) Marangoni convection is evident in n-octane droplets, and the vaporization rates are affected by the presence of Marangoni flows.

4) Because of the relatively large difference between the molecular weights of octane and air, buoyancy effects caused by the density gradients in presence of the gravitational field are very important for octane drops and results in larger evaporation rates, compared to the case of zero-gravity.

5) When high relative velocity between the drop and the surrounding air is present (for example, when droplets come out of an ejector), buoyancy and Marangoni effects may be negligible, compared to the convective effects related to the relative speed. However, Marangoni and buoyancy effects can be important in studies on evaporation or combustion of single stationary droplets.

Separation of the Marangoni and buoyancy effects can be achieved in a microgravity environment,[17,18] even though real zero-gravity conditions cannot be obtained on space platforms because of the presence of quasi-steady and oscillatory residual accelerations.[16] An experiment along these lines is being considered for the International Space Station.

References

[1]Ranz, W. E., and Marshall, W. R., Jr., "Evaporation from Drops, Part I," *Chemical Engineering Progress*, Vol. 48, No. 3, 1952, pp. 141–146.

[2]Ranz, W. E., and Marshall, W. R., Jr., "Evaporation from Drops, Part II," *Chemical Engineering Progress*, Vol. 48, No. 4, 1952, pp. 173–180.

[3]Law, C. K., "Recent Advances in Droplet Vaporization and Combustion," *Progress in Energy and Combustion Science*, Vol. 8, 1982, pp. 171–201.

[4]Sirignano, W. A., "Fuel Droplet Vaporization and Spray Combustion Theory," *Progress in Energy and Combustion Science*, Vol. 9, 1983, pp. 291–322.

[5]Faeth, G. M., "Evaporation and Combustion of Sprays," *Progress in Energy and Combustion Science*, Vol. 9, 1983, pp. 1–76.

[6]Dwyer, H. A., "Calculations of Droplet Dynamics in High Temperature Environments," *Progress in Energy and Combustion Science*, Vol. 15, 1989, pp. 131–158.

[7]Chiang, C. H., Raju, M. S., and Sirignano, W. A., "Numerical Analysis of Convective, Vaporizing Fuel Droplet with Variable Properties," *International Journal of Heat and Mass Transfer*, Vol. 35, No. 5, 1992, pp. 1307–1324.

[8]Lozinski, D., and Matalon, M., "Thermocapillary Motion in a Spinning Vaporizing Droplet," *Physics of Fluids A*, Vol. 5, 1993, pp. 1596–1601.

[9]Haywood, R. J., Renksizbulut, M., and Raithby, G. D., "Transient Deformation and Evaporation of Droplets at Intermediate Reynolds Numbers," *International Journal of Heat and Mass Transfer*, Vol. 37, No. 2, 1994, pp. 1401–1409.

[10]Niazmand, H., Shaw, B. D., Dwyer, H. A., and Aharon, I., "Effects of Marangoni Convection on Transient Droplet Evaporation," *Combustion Science and Technology*, Vol. 103, 1994, pp. 219–233.

[11]Shih, A. T., and Megaridis, C. M., "Thermocapillary Flow Effects on Convective Droplet Evaporation," *International Journal of Heat and Mass Transfer*, Vol. 39, No. 2, 1996, pp. 247–257.

[12]Chao, D. F., and Zhang, N., "Effects of Evaporation and Thermocapillary Convection on Volatile Liquid Droplets," *Journal of Thermophysics and Heat Transfer*, Vol. 15, No. 4, 2001, pp. 416–420.

[13]Savino, R., Monti, R., and Alterio, G., "Drops Pushing by Marangoni Forces," *Physics of Fluids*, Vol. 13, No. 5, 2001, pp. 1513–1516.

[14]Monti, R., Savino, R., and Tempesta, S., "Wetting Prevention by Thermal Marangoni Effects: Experimental and Numerical Simulations," *European Journal of Mechanics/B Fluids*, Vol. 17, No. 1, 1998, pp. 25–32.

[15]Monti, R., Savino, R., Lappa, M., and Tempesta, S., "Behaviour of Drops in Contact with Pool Surfaces of Different Liquids," *Physics of Fluids*, Vol. 10, No. 11, 1998, pp. 2786–2796.

[16]Monti, R., Savino, R., Alterio, G., and Fortezza, R., "Experimental and Numerical Study of Thermovibrational Convection," *Journal of Thermophysics and Heat Transfer*, Vol. 13, No. 1, 1999, pp. 161–163.

[17]Gökalp, I., Chauveau, C., and Richard, J. R., "Droplet Vaporisation and Combustion in Microgravity," *Combustion Experiment During KC-135 Parabolic Flights*, ESA SP-1113, ESA Publ. Division–European Space Research and Technology Centre, Noordwijk, The Netherlands, 1989, pp. 25–36.

[18]Ronney, P. D., "Combustion Phenomena at Microgravity," *Physics of Fluids in Microgravity*, Taylor and Francis, Philadelphia, 2002, p. 371.

[19]Law, C. K., Chung, S. H., and Srinivasan, N., "Gas-Phase Quasi-Steadiness and Fuel Vapour Accumulation Effects in Droplet Burning," *Combustion and Flame*, Vol. 38, 1980, pp. 173–198.

[20]Patankar, S. V., *Numerical Heat Transfer and Fluid Flow*, Hemisphere, Washington, DC, 1980.